Acta Oceanol. Sin., 2023, Vol. 42, No. 9, P. 132–144
https://doi.org/10.1007/s13131-022-2118-x
http://www.aosocean.com
E-mail: ocean2@hyxb.org.cn

Impacts of channel dredging on hydrodynamics and sediment dynamics in the main channels of the Jiaojiang River Estuary in China

Yanming Yao[1], Xueqian Chen[1], Jinxiong Yuan[2], Li Li[1]*, Weibing Guan[1, 3]

[1] Ocean College, Zhejiang University, Zhoushan 316021, China

[2] Hangzhou Xi'ao Environmental Science and Technology Company Limited, Hangzhou, 310011, China

[3] State Key Laboratory of Satellite Ocean Environmental Dynamics, Second Institute of Oceanography, Ministry of Natural Resources, Hangzhou 310058, China

Received 24 July 2022; accepted 14 September 2022

Abstract

Channel dredging in estuaries increases water depth and subsequently impacts sediment dynamics and morphology. The Jiaojiang River Estuary is dredged frequently owing to heavy shipping demands. In this study, the effects of different dredging schemes on siltation were assessed through numerical modeling. The sediment model of the Jiaojiang River Estuary utilized an optimized bottom boundary layer model that considered the bed sediment grain size and fluid mud, and this model was calibrated using field data. Result reveal that channel dredging modifies the flow velocity inside and around the channel by changing the bathymetry; subsequently, this affects the residual current, bed stress, suspended sediment concentration, and sediment fluxes. Increasing the dredging depth and width increases the net sediment fluxes into the channel and dredging depth has a greater influence on the channel siltation thickness. When the dredging depth is 8.4 m or11.4 m, the average siltation thickness of the channel is 0.07 m or 0.15 m per mouth respectively. The parallel movement of the channel has small effects on the siltation volume during the simulation period. The sediment deposits in the channel primarily originates from the tidal flats, through bottom sediment fluxes. Vertical net circulation has a dominant impact on siltation because the difference of horizontal current of each layer on the longitudinal section of the channel increases, which intensifies the lateral sediment transport between the shoal and channel. The influence of vertical frictional dissipation on the lateral circulation at the feature points accounts for more than 50% before dredging, while the non-linear advective term is dominant after dredging. Tidal pumping mainly affects the longitudinal sediment fluxes in the channel. These results can be used for channel management and planning for similar estuaries worldwide.

Key words: sediment dynamics, channel dredging, bottom boundary layer, siltation, Jiaojiang River Estuary

Citation: Yao Yanming, Chen Xueqian, Yuan Jinxiong, Li Li, Guan Weibing. 2023. Impacts of channel dredging on hydrodynamics and sediment dynamics in the main channels of the Jiaojiang River Estuary in China. Acta Oceanologica Sinica, 42(9): 132–144, doi: 10.1007/s13131-022-2118-x

1 Introduction

The estuaries along the coast of the East China Sea are the most developed and most turbid coastal environments on earth, owing to the extreme magnitude of human activities associated with coastal engineering and natural forcing by rivers and tides. Channel dredging is one of the most common human activities in estuaries along the east coast of China. In order to maintain the minimum draft required for the navigation and maneuvering of the ship in the port, the waterway must be dredged to remove excess sediments (Mateo-Pérez et al., 2020; Žilinskas et al., 2020). While the fact that dredging causes siltation has been known for a long time. Dredging alters the topography of the estuary artificially, affecting the current and the transport of suspended sediment (Martelo et al., 2019), breaking the original dynamic balance, and leading to the channel siltation (Wu and Li, 2010). Siltation can be due to various physical conditions, including hydrodynamic conditions, sediment characteristics and dredging size (Ghosh et al., 2001). The changes in hydrodynamic conditions are responsible for most of the severe siltation (Nguyen et al., 2013). Channel's deepening and widening can increase the tidal range and decrease the tidal phase from the mouth to the head of the Tampa Bay (Zhu et al., 2015). The bottom boundary layer (BBL) plays an important role in the material exchange, sediment erosion, resuspension, and accumulation between the seabed and seawater (Wang et al., 2000). The study of the dynamics of suspended sediment in the BBL of an estuary is of great significance for better understanding the physical process of siltation. Gu (2018) proposed that a high suspended sediment concentration (SSC) at the bottom level, with low current velocity, was the primary factor for channel siltation in the Changjiang

---

Foundation item: The National Key Research and Development Program of China under contract No. 2020YFD0900803; the National Natural Science Foundation of China under contract Nos 41976157 and 42076177; the Science Technology Department of Zhejiang Province under contract No. 2022C03044; the State Key Laboratory of Satellite Ocean Environment Dynamics of the Ministry of Natural Resources of China under contract No. QNHX1807.

*Corresponding author, E-mail: lilizju@zju.edu.cn

River Estuary. Jin (2019) pointed out that transport of highly concentrated suspended sediment near the bottom of the shoal, driven by transverse flow near the bottom, was the predominant means of sediment exchange between the coastal shoal and channel. Shen et al. (2020) found the vertical and horizontal accumulation of net suspended sediment near the bottom of the high siltation area in the North Passage of the Changjiang River Estuary. However, the transport mechanisms of highly concentrated suspended sediment near the bottom, caused by dredging, are poorly understood.

Scientists and engineers are deeply interested in the characteristics and mechanism of channel back silting. Huang (2007) discussed the effect of channel depth and width on siltation using a two-dimensional sediment mathematical model. Zhao et al. (2014) studied the Yuanyuansha Channel in the Changjiang River Estuary and found that the increase in siltation after dredging was due to the increase in the height difference between the channel and shoal and the angle between the tidal current and channel. Obelcz et al. (2018) found that the sediment deposited in the dredging pits in the Mississippi River Delta mainly came from river-derived or resuspended sediment, and the other came from the damage of the pit wall. Liu et al. (2020) pointed out the low valley formed by dredging is conducive to rapid sediment capture.

The Jiaojiang River Estuary is a funnel-shaped macro-tidal estuary located in the east coast of China (Fig. 1a), with bay width increasing from 0.9 km at the bay node (Haimen Port) to 20 km at the mouth (Baisha to Langji Mountain section). The estuary is muddy, with the Taizhou Shoal in the south and the Nanyang Shoal in the north. Except for summer occurrences of typhoons and tropical storms, the estuary has energetic and asymmetric tides. Sheltered by the islands outside the bay mouth, the waves are small, with a significant wave height ($H_{1/10}$) generally less than 1.5 m at the Toumen Island (Li et al., 2015). The tides near the bay mouth are semidiurnal, and the maximum and average spring tidal ranges are 5.8 m and 4 m, respectively. At Haimen Port, the maximum tidal amplitude is greater than 6.3 m. The tidal wave is strongly distorted in the estuary. For example, at Hai-

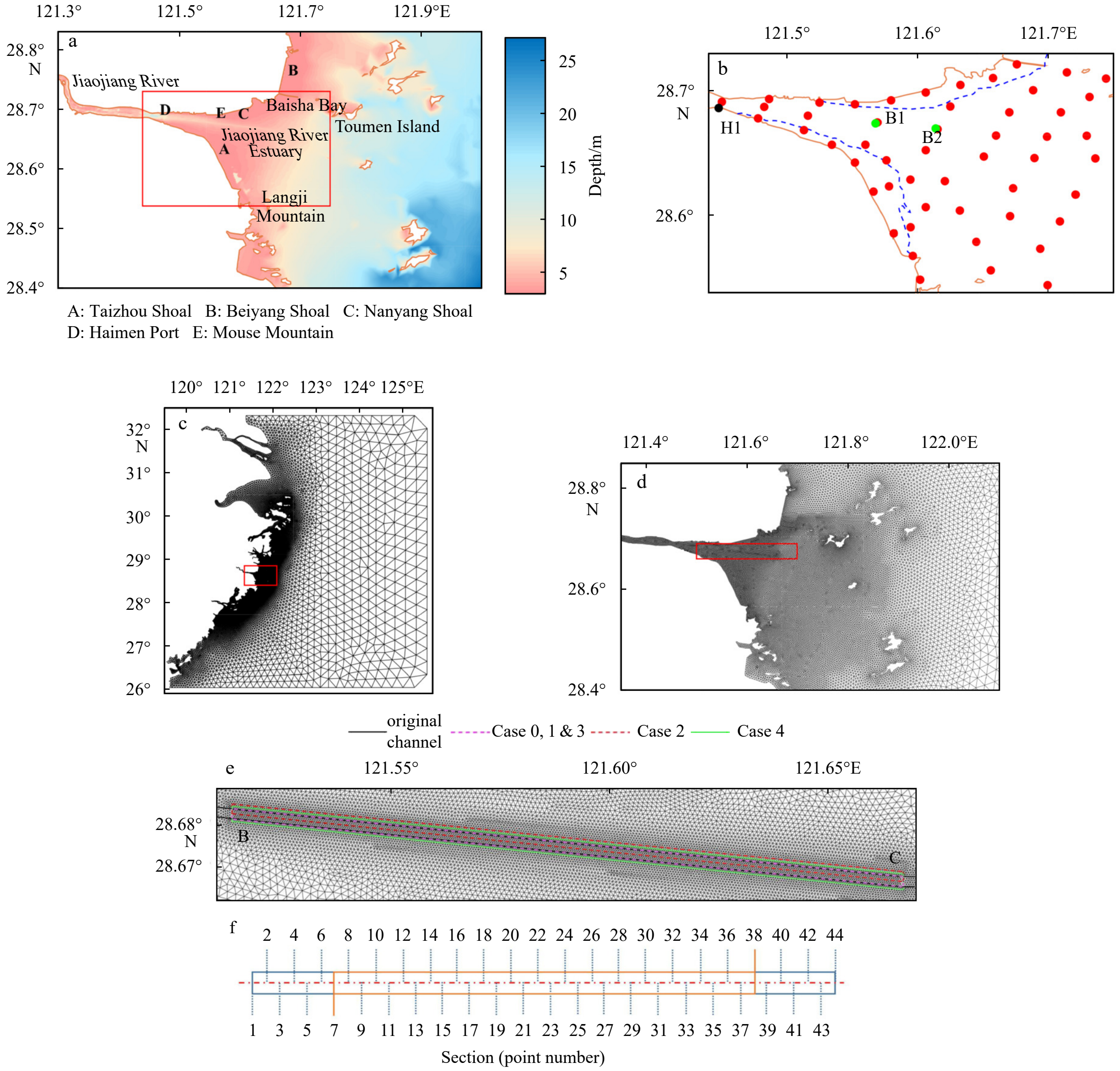

Fig. 1. Location of the Jiaojiang River Estuary (a); locations of bed sediment samples (red points) and field stations of the Jiaojiang River Estuary, H1 (Haimen station) is used for elevation observation, B1 and B2 are used for observation of currents and suspended sediment concentration in 2013 (b); model grids (c); grid around the Jiaojiang River Estuary (d); grid around the channel and location of channel dredging (e); distribution of characteristic points of channel center axis (f).

man Port, the flood tide lasts 5.1 h while the ebb tide lasts 7.3 h. The tidal currents also exhibit a similar asymmetry, with maximum flood and ebb tidal currents of 2.1 m/s and 1.8 m/s, respectively (Zhu, 1986). The annual average runoff and sediment discharge of the Jiaojiang River is 66.6×10^8 m^3 and 123.4×10^4 t, respectively. Upstream runoff has little effect on suspended sediment transport (Zhang, 2006). Compared to other factors, the tide dominates the sediment transport in the estuary. The siltation is caused predominantly by the tidal pumping effect, because of the asymmetric tidal current (Dong et al., 1997).

To maintain navigation depth, dredging is required every year in the Jiaojiang River Estuary (Li et al., 1992). The water depth near Haimen Port reaches 13 m, whereas that near the outer channel is only 4–6 m. The lack of water depth of the channel has seriously affected the expansion of the port scale. To meet the requirements of 5 000 dead weight tonnage (DWT) seagoing vessels and 10 000 DWT bulk carriers, the channel of the estuary needs to be expanded. Therefore, it is necessary to study the impact of channel dredging on the dynamic environment and its mechanism in the Jiaojiang River Estuary, so as to provide a reliable basis for estuary management.

The aims of this study is firstly to investigate the influence and mechanism of channel dredging on hydrodynamics and sediment dynamics, and secondly to discuss the source of silted sediment in the channel after dredging. This paper is structured as follows. The methodology is described and model validation is detailed in Section 2. Section 3 discusses the impacts of channel dredging in a short time on hydrodynamic and sediment dynamics under different dredging schemes of width, depth, and location. The mechanism of channel siltation based on the theory of estuarine dynamics and sediment dynamics is analyzed in Section 4. Conclusions are presented in Section 5.

2 Methodology

2.1 *Numerical model construction and calibration*

2.1.1 *Model description*

Based on the finite volume coastal ocean model (FVCOM) (Chen et al., 2003) and estuarine suspended sediment model (Wang, 2002), a three-dimensional numerical model of the hydrodynamics and sediment dynamics in the Jiaojiang River Estuary was established. The FVCOM is used to simulate the hydrodynamics, which uses an unstructured mesh and is suited to identify the complex geometry of the Jiaojiang River Estuary. The estuarine suspended sediment model focuses on suspended sediment dynamics, particularly in the sediment at the bottom boundary layer (BBL). The model considered the two-way coupling of the suspended sediment concentration (SSC) and water density, the effect of fluid mud at the BBL, and the fine sediment flocculation (Ye et al., 2019). Sediment processes are parameterized as follows:

$$\frac{\partial\left(C\right)}{\partial t}+\frac{\partial\left(uC\right)}{\partial x}+\frac{\partial\left(vC\right)}{\partial y}+\frac{\partial\left(\left(w-w_{\rm s}\right)C\right)}{\partial z}= \frac{\partial}{\partial x}\left(A_{\rm h}\frac{\partial C}{\partial x}\right)+\frac{\partial}{\partial y}\left(A_{\rm h}\frac{\partial C}{\partial y}\right)+\frac{\partial}{\partial z}\left(K_{\rm h}\frac{\partial C}{\partial z}\right), \tag{1}$$

where u, v, and w (m/s) are the x, y, z velocity components; C (kg/m^3) is the SSC; w_s is the settling velocity of suspended sediment, which is positive in the downward direction; K_h is the vertical sediment mixing coefficient; A_h is the horizontal sediment mixing coefficient.

The boundary conditions of suspended sediment fluxes at the surface level and bottom level of the model are as follows:

$$-w_{\rm s}C-K_{\rm h}\frac{\partial C}{\partial z}=0,\ z=\zeta, \tag{2}$$

$$-w_{\rm s}C-K_{\rm h}\frac{\partial C}{\partial z}=E-D,\ z=-h, \tag{3}$$

where E is the sediment resuspension flux; D is the suspended sediment deposition flux at the bottom level; ζ is the height of the free surface (relative to $z = 0$) and h is bottom depth (relative to $z = 0$).

The sediment resuspension flux (E) is calculated using van Prooijen's formula (van Prooijen and Winterwerp, 2010),

$$E=\begin{cases}0,\ \tau_{\rm b}<0.52\tau_{\rm ce}\\ E_0\left(1-P_{\rm b}\right)\left[-0.144\left(\dfrac{\tau_{\rm b}}{\tau_{\rm ce}}\right)^3+0.904\left(\dfrac{\tau_{\rm b}}{\tau_{\rm ce}}\right)^2-\right.\\ \left.0.823\dfrac{\tau_{\rm b}}{\tau_{\rm ce}}+0.204\right],\ 0.52\tau_{\rm ce}\leqslant\tau_{\rm b}\leqslant1.70\tau_{\rm ce}\\ E_0\left(1-P_{\rm b}\right)\left(\dfrac{\tau_{\rm b}}{\tau_{\rm ce}}-1\right),\ \tau_{\rm b}>1.70\tau_{\rm ce}\end{cases}, \tag{4}$$

where E_0 is the sediment erosion rate, P_b is the porosity, τ_b is the bottom shear stress, and τ_{ce} is the critical shear stress for sediment erosion.

The τ_b value is expressed as follows:

$$\tau_{\rm b}=\rho C_{\rm d}\left|u_{\rm b}\right|u_{\rm b}, \tag{5}$$

where u_b is the current velocity at the bottom level, ρ is the water density, and C_d is the bottom friction coefficient.

The water density is determined by considering the effect of SSC (Winterwerp, 2001) as follows:

$$\rho=\rho_{\rm w}+\left(1-\frac{\rho_{\rm w}}{\rho_{\rm s}}\right)C, \tag{6}$$

where ρ_w is the density of water without considering the sediment, and ρ_s is the sediment density.

Most of the suspended sediment particles in the Jiaojiang River Estuary are fine-grained silty clay; flocculation occurs easily in an environment with high SSC, so a flocculation setting is considered in the settling velocity of the sediment (Xu et al., 2018),

$$w_{\rm s}=w_{\rm s0}\frac{1+4.6C^{0.6}}{1+0.06U^{0.75}}\times1.3, \tag{7}$$

where w_{s0} is the settling velocity of a single particle calculated using Stokes' settling velocity formula; U is the current velocity of each layer.

The bottom friction coefficient is generally small in the muddy coast, where tidal current is the major driver, but it has a great impact on the SSC. In this study, the effect of fluid mud on bottom stress was considered as follows (Wang et al., 2005; Wang, 2002):

$$C_{\rm d}=\frac{k^2}{\left(1+AR_{\rm f}\right)^2\left[\ln\left(1+h/z_0\right)-1\right]^2}, \tag{8}$$

where $k = 0.4$ is the von Karman constant, A is an empirical coefficient set to 5.5, R_f is the flux Richardson number, h is the water depth, and z_0 is the bottom roughness length.

z_0 is related primarily to the particle size of the bed sediment. Most median particle sizes in the study area were approximately 0.007 mm. When $d_{50} < 0.5$ mm, $z_0 = 0.001$ m or $z_0 = nd_{50}$ (median sediment particle size) (Dong and Zhang, 2011). Comparing the differences between the modeled SSC values and observed SSC values for different z_0, the bed roughness length in the Jiaojiang River Estuary was set to $z_0 = 1d_{50}$.

2.1.2 *Model configuration*

The model domain covers the the entire Jiaojiang River Estuary ranging from the upstream to the outer sea (26.0°–32.3°N, 119.6°–125.6°E). The unstructured triangular grids of the model domain consisted of 95 149 elements and 49 644 nodes (Fig. 1c), with the element sizes ranging from 30 km (of the open-ocean boundary) to 200 m (of the study area of the Jiaojiang River Estuary; Fig. 1d). The grid resolution near the channel was approximately 50 m (Fig. 1e). Figure 1f depicts 44 characteristic points selected along the channel, of which ponit 7 and point 38 (Fig. 1f) are at the landward and seaward end of the channel, respectively. The distance between each pair of consecutive points was 500 m.

The open-boundary conditions for the water level were specified using tidal elevations predicted by the TPXO7.2 global model of ocean tides (Egbert et al., 2010). Hourly tidal elevations—K_1, O_1, P_1, Q_1, M_2, S_2, N_2, K_2, M_4, MS_4, MN_4, M_f, and M_m—were applied to the open-ocean boundary. The model employed a cold start, and the initial velocity and tide level were both zero.

Two major rivers—the Jiaojiang River and the Changjiang River—discharge into this region. Hence, river discharge was considered in the model. The wind in the Jiaojiang River Estuary is small, so the factors of wind and waves at the free-surface boundary were neglected in the model, to focus on the near-bottom sediment dynamics. The model was initialized with constant values of salinity (25) and temperature (18℃). The key parameters of the model are summarized in Table 1.

Seven scenarios (Case 0–Case 6; Table 2) were designed to study the effect of dredging on hydrodynamics and sediment dynamics in the estuary. Case 0 was the control run without the channel dredging, and it was calibrated using field data. For Case 1, channel dredging was performed, with a channel length of 15.5 km, depth of 8.4 m, and width of 250 m according to the requirements of ship type. In Case 2, the dredged channel was moved 125 m to the north compared to Case 1, which is convenient for navigation during construction. The channel was deepened to 11.4 m in Case 3 and widened to 400 m in Case 4. In addition, the channel was deepened to 9.4 and 10.4 in Case 5 and Case 6 respectively to further discuss the impacts of channel deepening. The cross-section of the dredged channel was trapezoidal; the ratio of the slopes of the north and south sides of the dredged channel was 1:10, and that of the east and west sides was 1:50.

Table 1. Key parameters of the model

Model parameter	Value
Node, element, and vertical layers	49 644 nodes, 95 644 elements, and 5 uniform σ layers
External time step	0.1 s
Internal time step	1 s
Open boundary condition	sea surface elevation time series from TPXO7.2
Porosity of sediment	0.5
Bed roughness length	0.007 mm
Critical stress for resuspension	0.2 N/m²
Erosion rate	0.000 6 kg/(m²·s) (Wang, 2007)
Settling velocity of particle	0.2 mm/s (Zhang, 2006)

Table 2. Basic dredging statistics

Experiment	Location	Length/km	Depth/m	Width/m
Case 0	ND	ND	ND	ND
Case 1	BC	15.5	8.4	250
Case 2	north side of BC	15.5	8.4	250
Case 3	BC	15.5	11.4	250
Case 4	BC	15.5	8.4	400
Case 5	BC	15.5	9.4	250
Case 6	BC	15.5	10.4	250

Note: BC represents central axis in Fig. 1e. ND: non-dredging.

2.1.3 *Model validation*

The tidal elevation data were measured hourly by TGR-2050 Automated Tide Gauge, were observed from 00:00 on August 16, 2014 to 23:00 on September 9, 2014 at the Haimen Station (H1) (Fig. 1b). The tidal current data were measured hourly by SLC9-2 Direct Reading Current Meter during a spring tide (9–10 July, 2013) at the surface, bottom, and middle levels at Stations B1 and B2 (Fig. 1b). Suspended sediment was sampled hourly by XCL Horizontal Sampler for the same time in 2013. And SSC data were measured by Drying-Weighing Method.

Correlation coefficient (CC) (Eq. (9)) and skill score (SS) (Eq. (10)) was used to evaluate the accuracy of the model:

$$\mathrm{CC} = \frac{1}{N}\sum_{i=1}^{N}\frac{(m_i - \overline{m})\left(O_i - \overline{O}\right)}{S_{\mathrm{m}}S_{\mathrm{o}}}, \tag{9}$$

$$\mathrm{SS} = 1 - \frac{\sum\limits_{i=1}^{N}(m_i - O_i)^2}{\sum\limits_{i=1}^{N}\left(O_i - \overline{O}\right)^2}, \tag{10}$$

where m_i is the value calculated from the model; O_i is the observed value; $\overline{m}$ and $\overline{O}$ are the average values of the calculation and observation, respectively; S_{m} and S_{o} are the standard deviations of the calculation and observation, respectively.

Verification of tide levels revealed the simulations to be in good agreement with the observations (Fig. 2a). The CC value is 0.98, and SS value is 0.96. Figures 2b and c illustrates the comparison between the observed and modeled current velocities and directions near the surface, middle, and bottom levels at Stations B1 and B2 Stations during the spring tides. The CC and SS values of velocity in each layer are greater than 0.97 and 0.91 respectively. And those of current direction in each level are greater than 0.75 and 0.44. Therefore, the hydrodynamic model is reliable and can reproduce the characteristics of the tidal levels and tidal currents. Regarding verification of the SSC (Fig. 2d), the CC and SS values are greater than 0.43 and 0.30 at the two stations respectively, although some errors exist between the simulations and observations, the overall magnitudes and trends are generally consistent. Thus, the sediment model is reliable and can effectively simulate the sediment process.

2.2 *Sediment flux decomposition*

Channel dredging changes the sediment dynamics and sub-

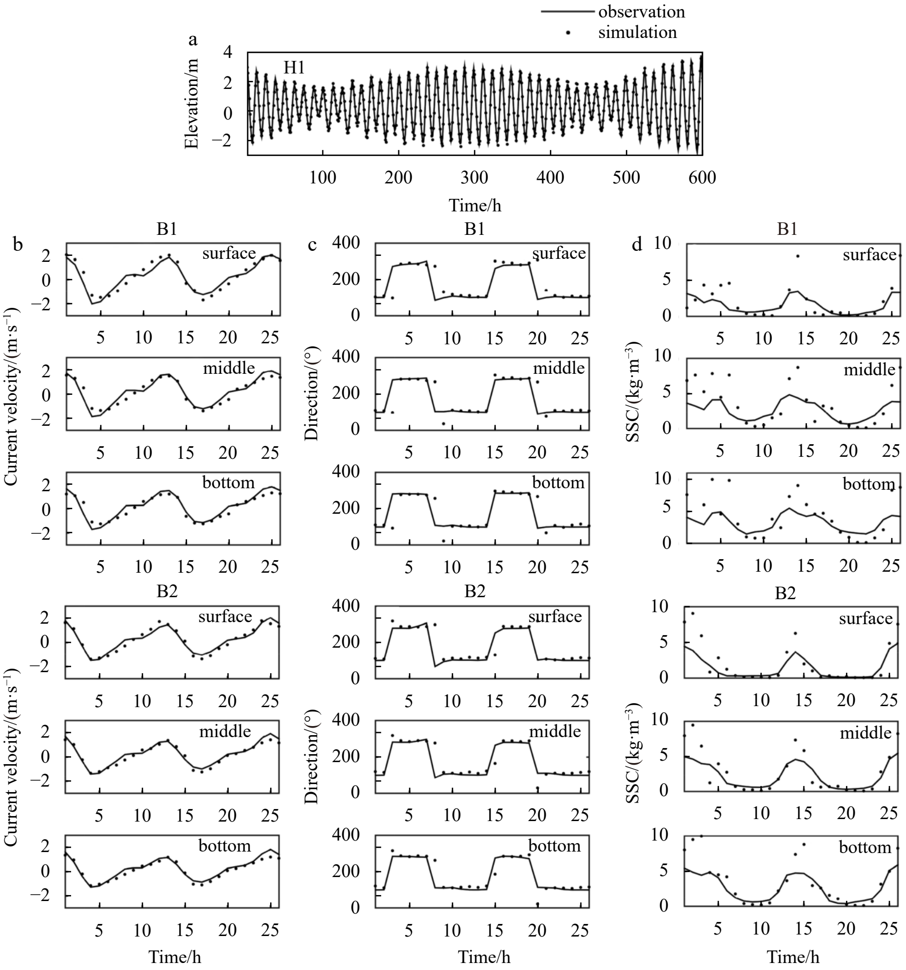

Fig. 2. Comparison between observed and modeled elevations at Haimen station (H1) (a), current velocities and directions during the spring tides at B1 and B2 stations (b, c), and suspended sediment concentration (SSC) during the spring tides at B1 and B2 stations (d).

sequently impacts siltation. We used Dyer’s (1997) flux decomposition method to analyze the sediment flux and its changes after channel dredging. This method can be used to calculate each decomposition term of a tidal period. The current velocity and SSC are decomposed into a vertical mean term and its deviation term; then, the mean term is decomposed into tidal mean and tidal oscillation terms. This can be expressed as follows:

$$
\begin{aligned}
\langle F\rangle =& \frac{1}{T}\int_0^T\int_0^h uc\mathrm{d}z\mathrm{d}t = \frac{1}{T}\int_0^T\int_{-1}^0 huc\mathrm{d}\sigma\mathrm{d}t = \\
& h_0\overline{U}_0\overline{C}_0 + \overline{C}_0\left\langle h_{\mathrm{t}}\overline{U}_{\mathrm{t}}\right\rangle + \overline{U}_0\left\langle h_{\mathrm{t}}\overline{C}_{\mathrm{t}}\right\rangle + \\
& h_0\left\langle \overline{U}_{\mathrm{t}}\overline{C}_{\mathrm{t}}\right\rangle + \left\langle h_{\mathrm{t}}\overline{U}_{\mathrm{t}}\overline{C}_{\mathrm{t}}\right\rangle + h_0\left\langle \overline{U_{\mathrm{v}}C_{\mathrm{v}}}\right\rangle + \left\langle h_{\mathrm{t}}\overline{U_{\mathrm{v}}C_{\mathrm{v}}}\right\rangle = \\
& T_1 + T_2 + T_3 + T_4 + T_5 + T_6 + T_7
\end{aligned} \qquad (11)
$$

where the bracket denotes the average tide period; the overbar indicates the vertical average; U_{v} and C_{v} are the deviations of the velocity and SSC, respectively, at each level relative to the vertical average value. $\overline{U}_0$ and $\overline{C}_0$ are the average vertical velocity and SSC of the time average, respectively; $\overline{U}_{\mathrm{t}}$ and $\overline{C}_{\mathrm{t}}$ are the deviations of the vertical average velocity and SSC, respectively, relative to $\overline{U}_0$ and $\overline{C}_0$. h_0 is the average water depth over time, h_{t} is the deviation term of water depth relative to h_0 at each time. $T_1 + T_2$ is the advection sediment transport caused by Euler residual current and mass-transport Stokes residual current; $T_3 + T_4 + T_5$ represents the tidal pumping effect produced by the tidal phase differences; $T_6 + T_7$ is the vertical net circulation transport, caused by the difference in the velocity and vertical distribution of SSC during a tide cycle, T_6 is due to the circulation current with high sediment concentration at the bottom level and low sediment concentration at the surface level, and T_7 arises from the changing forms of the vertical profiles of current velocity and SSC.

Since lateral circulation plays an important role in lateral suspended sediment transport, we used the method described in Kalkwijk and Booij (1986) to examine the dynamic mechanism for lateral circulation. Equation (12) decomposes the time rate of change of the lateral velocity.

$$
\begin{aligned}
\frac{\partial U_{\mathrm{n}}}{\partial t} =& \left[-\left(U_{\mathrm{s}}\frac{\partial U_{\mathrm{n}}}{\partial s} - \overline{U_{\mathrm{s}}\frac{\partial U_{\mathrm{n}}}{\partial s}}\right) - \left(U_{\mathrm{n}}\frac{\partial U_{\mathrm{n}}}{\partial n} - \overline{U_{\mathrm{n}}\frac{\partial U_{\mathrm{n}}}{\partial n}}\right)\right] - \\
& \left(fU_{\mathrm{s}} - \overline{fU_{\mathrm{s}}}\right) + \left(\frac{U_{\mathrm{s}}^2}{R_{\mathrm{s}}} - \overline{\frac{U_{\mathrm{s}}^2}{R_{\mathrm{s}}}}\right) - \\
& \left(\frac{g}{\rho_0}\int_z^0 \frac{z'\partial\rho}{\partial n}\mathrm{d}z' - \overline{\frac{g}{\rho_0}\int_z^0 \frac{z'\partial\rho}{\partial n}\mathrm{d}z'}\right) + \\
& \left[\frac{\partial}{\partial z}\left(K_{\mathrm{m}}\frac{\partial U_{\mathrm{n}}}{\partial z}\right) - \overline{\frac{\partial}{\partial z}\left(K_{\mathrm{m}}\frac{\partial U_{\mathrm{n}}}{\partial z}\right)}\right]
\end{aligned}, \qquad (12)
$$

where U_n and U_s are the velocity in longitudinal and lateral directions, respectively; f is Coriolis coefficient; R_s is radius of curvature. The terms on the right of Eq. (11) are nonlinear advection of the longitudinal momentum, nonlinear advection of the lateral momentum, the Coriolis force, the centrifugal force, the lateral baroclinic pressure gradient, and the vertical frictional dissipation. Since $w \ll U_n$, and $w \ll U_s$, the advection of the lateral momentum in the vertical direction was omitted.

Tidal asymmetry refers to that combination of tidal components of different frequencies leading to an unequal duration of the rising and falling tides, as well as a difference between the duration and strength of the flood and ebb tidal current. In shallow water, the M_2/M_4 combination is often the main cause of tidal asymmetry (Aubrey and Speer, 1985), other constituent combinations only played minor roles. If only these two constituents are considered, tidal asymmetry can be calculated with the following formula (Song et al., 2011).

$$\gamma_{M_2/M_4} = \frac{\dfrac{3}{2} a_{M_2}^2 a_{M_4} \sin\left(2\varphi_{M_2} - \varphi_{M_4}\right)}{\left[\dfrac{1}{2}\left(a_{M_2}^2 + 4a_{M_4}^2\right)\right]^{\frac{3}{2}}}, \tag{13}$$

where a and φ are the tidal amplitudes and phases of the components of the astronomical tides, respectively.

3 Results

3.1 *Grain size of bed sediments*

3.1.1 *Sample collection and grain size analysis*

Fifty-one bed sediment samples were collected using a thin-walled sampler at a height of 0.4 m in the surface layer of the bottom bed at the Jiaojiang River Estuary on September 10, 2014. The locations of the samples covered the area from Haimen Port to the bay mouth (Fig. 1b). The samples were treated with 6% H_2O_2 to remove organic matter. The sediment samples were analyzed using the Mastersizer 3000 in the laboratory to get grain size. The sediments were classified following the classification provided by Folk (Folk et al., 1970). The bed sediment grain sizes were used in designing the BBL scheme of the numerical model.

3.1.2 *Grain size of bed sediment*

Examination of the 51 sediment samples reveals that mainly fine-grained sediments are present in the Jiaojiang River Estuary during the fieldwork period, composed primarily of sandy clay and clayey silt (Fig. 3a).

Sandy clay is the predominant sediment type in the Jiaojiang River Estuary, which is distributed from the Haimen Port to the Mouse Mountain, Taizhou Shoal, and south of the estuary. The clay content is more than 50% and the silt content is between 30% to 49%.

Clayey silt is distributed in the Nanyang Shoal and scattered in the Taizhou Shoal and near the bay mouth of the estuary. The silt content is more than 50%, and the clay content is between 28% to 47%.

The median sediment grain size in the Jiaojiang River Estuary ranges from 0.004 mm to 0.013 mm (Fig. 3b), with peak values occurring near the southern shoal. The median grain size generally decreases from the bay head to the bay mouth and increases from the northern bank to the southern bank. The median grain size near the Nanyang Shoal and near the mouth of the estuary is larger, and the corresponding sediment type is clayey silt. The median grain size is small in the Taizhou Shoal and south of the estuary.

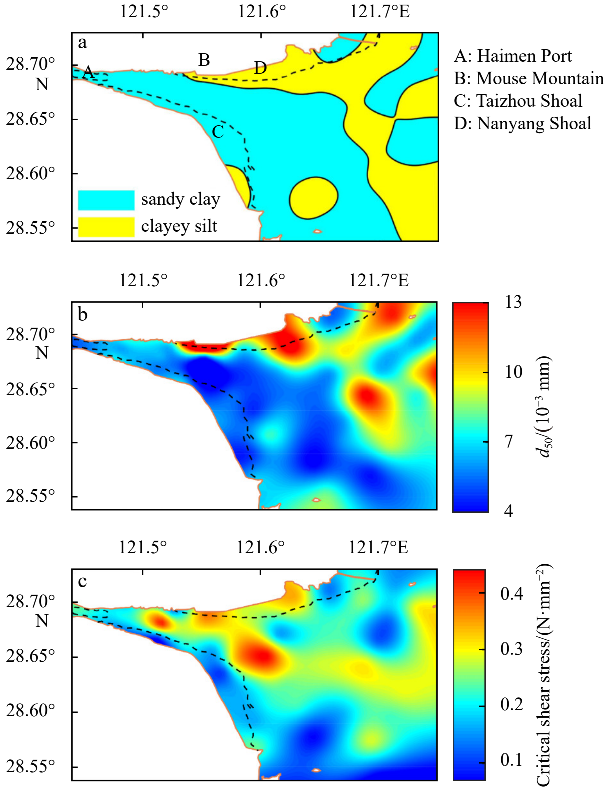

Fig. 3. Distribution of bed sediment types (a), median grain size (d_{50}) (b), and critical shear stress (τ_{ce}) (c) in the Jiaojiang River Estuary.

3.1.3 *Critical shear stress calculation of bed sediment*

The critical stress for resuspension (τ_{ce}) in the Jiaojiang River Estuary was estimated through the following formula (Dou, 1999):

$$\tau_{ce} = k^2 \rho \left(\frac{d'}{d^*}\right)^{\frac{1}{3}} \left\{ 3.6 \frac{\rho_s - \rho_w}{\rho_w} g d_{50} + \left(\frac{\gamma_0}{\gamma_{0^*}}\right)^{2.5} \times \left[\frac{\varepsilon_0 + gh\delta(\delta/d_{50})^{0.5}}{d_{50}}\right] \right\}, \tag{14}$$

where k is 0.128; g is the acceleration of gravity; d_{50} is the median sediment particle size; ε_0 is the cohesive force parameter, which is 1.75; h is the water depth; δ is the film water thickness, set to 2.31×10^{-5} cm; d^* is 10 mm; d' is the rough height, set to 0.5 mm; γ_0 is the dry bulk density of the bed sediment; γ_0^* is the stable dry bulk density of sediment particles, which is set to 1.43 for silt and 1.37 for clay.

The distribution of τ_{ce} in the estuary is shown in Fig. 3c. The range of τ_{ce} is 0.07–0.44 N/mm^2, and the values of τ_{ce} in most areas of the estuary are between 0.1–0.3 N/mm^2. In general, τ_{ce} in the deep-water area outside the Taizhou Shoal and the Jiaojiang River Estuary is small, whereas in the south of the Mouse Mountain and the side of the Nanyang Shoal, the parameter is larger. The bottom stress scheme depicted in Fig. 3c is used in the numerical model of the Jiaojiang River Estuary (Table 1).

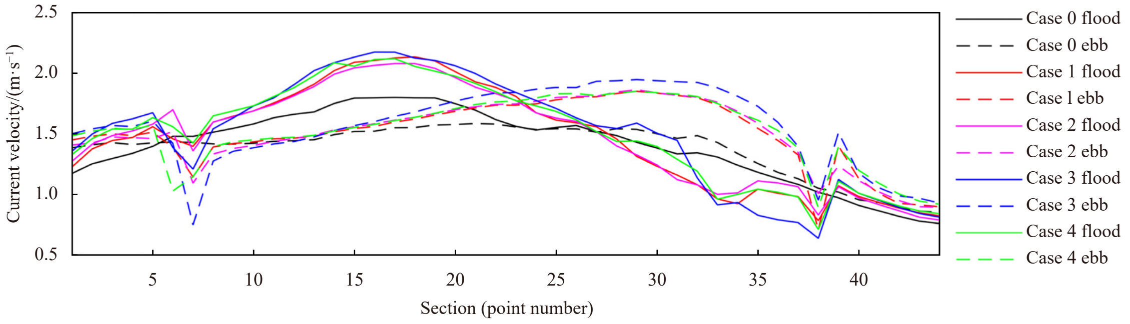

Fig. 4. Variation in current velocity of channel central axis at the bottom level for Case 0–Case 4 during the spring and ebb peak tides.

3.2 *Influence of dredging on current velocities and SSCs*

Figure 4 illustrates the variations in the bottom currents at the channel central axis during the spring tides, highlighting the impact of dredging on the currents. After dredging, currents are concentrated in the channel, the tidal prism of the shoals on the north and south sides decreases, so the current magnitudes there generally decrease. The largest decrease in current magnitudes is exhibited in Case 3 (deepening). The current directions are determined chiefly by the channel morphology.

During the spring tides, the tidal currents are asymmetric in the channel; the maximum flooding currents are stronger/weaker than ebbing currents in the landward/seaward section of the channel. After dredging, the current asymmetry in the channel increases. In addition, for Case 1–Case 4, the maximum peak flood velocity at the landward section of the channel increases significantly, by 0.33 m/s, 0.28 m/s, 0.37 m/s, and 0.32 m/s, respectively, and the maximum peak ebb velocity at the seaward section increases by 0.27 m/s, 0.28 m/s, 0.36 m/s, and 0.27 m/s, respectively. However, the maximum velocity decreases by 0.08 m/s, 0.12 m/s, 0.27 m/s, and 0.06 m/s, respectively, in the peak flood condition; it decreases by 0.29 m/s, 0.33 m/s, 0.68 m/s, and 0.30 m/s, respectively, during the peak ebb condition at the upstream location outside the channel (Point 7) (Fig. 4). The velocity decreases by 0.24 m/s, 0.19 m/s, 0.38 m/s, and 0.20 m/s, respectively, for Case 1–Case 4, during peak flooding and decreases by 0.34 m/s, 0.04 m/s, 0.20 m/s, and 0.16 m/s, respectively, during peak ebbing at the downstream location outside the channel (Point 38) (Fig. 4).

During the neap tides (figure not shown), the current asymmetry is weaker than that in the spring tides. After dredging, the current velocity in the channel decreases along the seaward side, except at both ends of the channel. On the channel axis, the maximum decrease in the peak flood velocity is 4%–9%, and the maximum increase in the peak ebb velocity is 6%–13%, for Case 1–Case 4.

Figure 5 illustrates the variation in vertically averaged SSC near the bottom level and the bottom shear stress during the spring tides, to study the impacts of channel dredging on the SSC and bottom shear stress. The bottom shear stress is important to estuarine sediment dynamics and erosion–deposition processes (Zhu et al., 2014). During the spring tides, the dredging induces a decrease in the bottom shear stress in the northern and southern shoals of the channel. Although currents in the channel weakens at the flood and ebb peaks, the bottom shear stress decreases with an increase in water depth. The bottom shear stress at the upstream and downstream sections outside the channel increases, and it also increases at the interface between the channel and shoal. The variation in the SSC and bottom shear stress during the neap tides (figure not shown here) is similar to that during the spring tides.

In general, the temporal and spatial variation of the SSC follows a pattern similar to that of the bottom shear stress. During the spring tides, for Case 1–Case 4, the maximum decrease in the SSC in the northern and southern shoals of the estuary reaches 0.36 kg/m^3, 0.38 kg/m^3, 0.59 kg/m^3, and 0.49 kg/m^3, respectively. However, although the bottom shear stress in the channel decreases, the SSC in the channel decreases little or even increased owing to sediment advection from interface between the channel and shoal. Besides, the change of the bottom shear stress is consistent with SSC at the upstream and downstream sections outside the channel, which also increases.

3.3 *Influence of dredging on residual currents and sediment fluxes*

The Euler residual current and mass-transport Stokes residual current constitute the residual transport current (Wu et al., 2014), which reflects the amount and direction of net water transport and plays an important role in sediment transport,

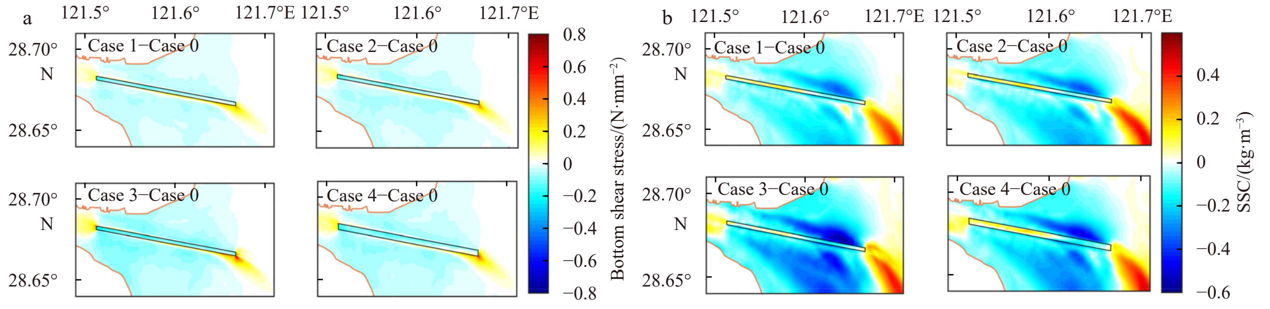

Fig. 5. Variation in bottom shear stress (a), and suspended sediment concentration (SSC) (b) at the bottom level of Cases 1–4–Case 0 during the spring tides.

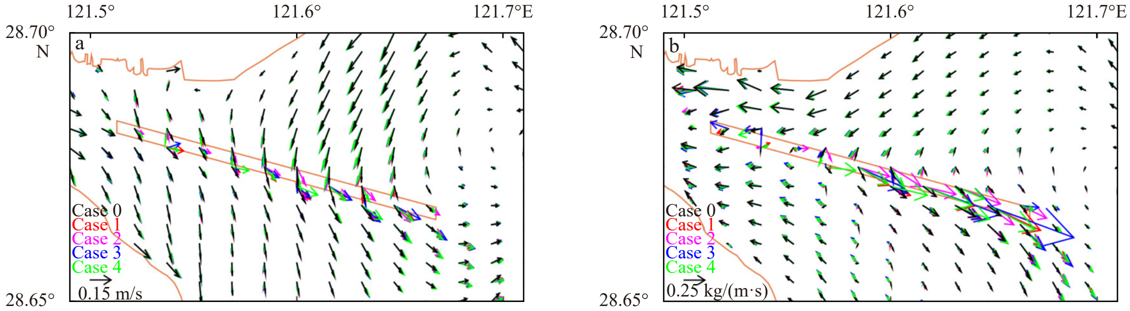

Fig. 6. Distribution of monthly averaged residual current (a), and net sediment fluxes per unit width (b) at the bottom level for Case 0–Case 4.

$$\overline{U}_{\mathrm{L}} = \overline{U}_{\mathrm{E}} + \overline{U}_{\mathrm{S}} = \overline{U}_0 + \frac{\langle h_{\mathrm{t}} U_{\mathrm{t}}\rangle}{h_0}, \qquad (15)$$

where $\overline{U}_{\mathrm{E}}$ is the Euler residual current and $\overline{U}_{\mathrm{S}}$ is the mass-transport Stokes residual current.

The residual currents near the bottom level which entered the channel are mainly from the upstream section and the northern shoal of the estuary (Fig. 6a). They cross the channel and flows from the northern shoal to the southern shoal. After dredging, the residual currents at the northern shoal of the estuary are deflected to the inside of the channel. Near the southern bank of the channel, they flows to the downstream section of the channel. Owing to the channel bathymetry, the residual currents are diverted to the south and east directions in the northern shoal of the estuary and near the dredged channel, whereas they remains unchanged in the southern shoal. In addition, the variations in residual currents for Case 3 (deepening) and Case 4 (widening) are larger than those for Case 1 (dredging controlled) and Case 2 (moving). A more detailed analysis of the residual currents is presented in Section 4.2.

In general, net sediment flux transport is responsible for morphological changes (Guo et al., 2014). The distribution of monthly averaged sediment fluxes at the bottom level is presented in Fig. 6b. Near the downstream section of the channel, the net sediment fluxes at the north and south shoals decrease significantly owing to the decrease in current velocity, while the transport components into the channel increase. Meanwhile, the channel dredging enhance the sediment transport to the seaward end in the downstream section of the channel, suggesting increasing erosion at that end. Near the upstream end of the channel, the net sediment fluxes at the south shoal increase, leading to deposition at the landward end of the channel. Sediment near the landward of the channel is transported to the seaward end, and its magnitude also increases.

The suspended sediment entering the channel mainly originates from the sediment transport at the bottom level. Sediment fluxes at the bottom level are presented in Table 3. The variation in sediment fluxes after dredging is more severe during the spring tides. For the sediment transported to the inside of the channel during this period, the flux quantity increases significantly compared to Case 0 (non-dredging), especially for Case 3 (deepening). During the neap tides, the net sediment entering into the channel increases, also with the peak increase occurring in Case 3 (deepening). The cumulative data of one month reveal that the sediment fluxes for Case 3 (deepening, 1 928 kg/s) are larger compared to other cases. The sediment fluxes for Case 1 (dredging controlled), Case 2 (moving), and Case 4 (deepening) are smaller—1 075 kg/s, 1 024 kg/s, and 1 045 kg/s, respectively. Compared to the north and south sections, the monthly averaged sediment fluxes of the east and west sections are smaller, with a contribution of less than 8.3%.

4 Discussion

4.1 *Siltation in the estuarine channels*

Due to the variation of hydrodynamic conditions near the dredged channel, the seabed is readjusted and there occurs scouring and silting. The seaward and landward ends of the channel, channel's north and south shoals, as well as the seabed near the upstream and downstream of the channel are scoured. Since the sediment at the interface between the channel and shoals is transported to the inside of the channel with the muddy water crossing the channel, scour also occurs here. Conversely, siltation occurs inside the channel. The different depth, width, and location of estuarine channels result in different siltation. For a channel situated at a certain location, the siltation thickness increases with the increase of dredging width and depth. Average siltation thickness in the channel of Case 1 (dredging controlled) within one month is 0.07 m. When the dredging depth increases, the siltation thickness increases by 0.15 m, 0.11 m and 0.13 m, respectively, in Case 3 (deepening by 11.4 m), Case 5 (deepening by 9.4 m) and Case 6 (deepening by 10.4 m). In Case 4 (widening) and Case 2 (moving), it is 0.08 m and 0.06 m, respectively, less siltation than the deepening cases (Fig. 7a). Compared with oth-

Table 3. Net sediment fluxes at the bottom level: spring tide cycle-average, neap tide cycle-average, and monthly average values for the four sections

	Spring tide cycle-average value/(kg·s^{-1})					Neap tide cycle-average value/(kg·s^{-1})					Monthly average value/(kg·s^{-1})				
	N	S	W	E	T	N	S	W	E	T	N	S	W	E	T
Case 0	1 059	−967	−68	−52	−28	25.5	−7.9	−2.9	0.2	15.0	409	−349	−16	−15	29
Case 1	2 270	301	−80	−129	2 362	48.7	31.4	−0.4	0.4	80.1	919	212	−18	−38	1 075
Case 2	2 180	302	−72	−127	2 283	46.0	27.8	−1.0	0.4	73.1	883	198	−20	−37	1 025
Case 3	3 380	1 660	−142	−206	4 693	58.8	54.0	−2.2	0.4	111.0	1 329	717	−44	−73	1 929
Case 4	2 151	308	−121	−224	2 113	54.2	34.8	1.2	0.5	90.7	876	256	−24	−63	1 045

Note: N: north section, S: south section, W: west section, E: east section, T: total. Positive value indicates the transport of suspended sediment into the channel, while negative value is opposite.

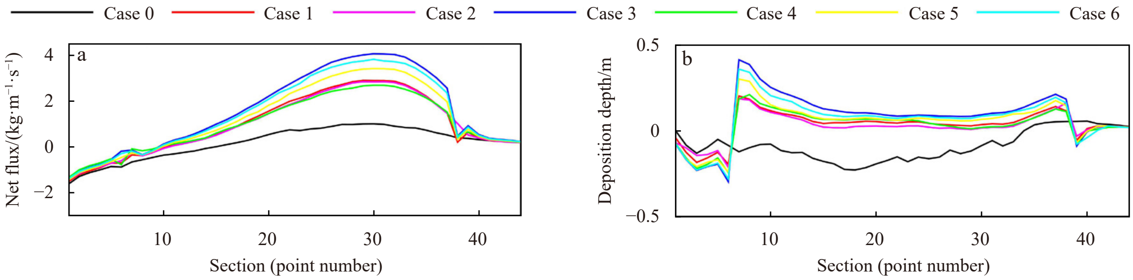

Fig. 7. Distribution of monthly averaged net sediment fluxes per unit width along the channel central axis (positive values indicate transport towards the downstream) (a); distribution of silting thickness along the channel central axis in one month (b).

er schemes, the elevation difference of Case 2 (moving) between the north section of the channel and the northern shoal of the estuary increases, whereas that between the south section and the southern shoal decreases. The magnitude of increment of the former is greater than the magnitude of decrement of the latter. The total dredging volume increases by 8.6% compared to Case 1 (dredging controlled), but the siltation thickness is thinner. The current velocity of the northern shoal is lower, leading to the sediment fluxes into the channel from the north side being less than those for Case 1 (dredging controlled).

In terms of siltation and dredging ratio, Case 3 (deepening by 11.4 m) exhibits the largest value—4.21%, followed by Case 4 (widening)—4.18% and Case 1 (dredging controlled)—4.04%, and Case 2 (moving) presents the smallest value—only 2.83%. From the perspective of practical engineering, it is highly uneconomic to increase the dredging depth and width considerably for a dredging scale that is already suitable for current navigation planning. Both values of the average siltation thickness and siltation and dredging ratio for Case 2 (moving) is smallest, so Case 2 (moving) are more economical compared with other schemes. From the perspective of practical construction, for the dredging scale that is already suitable for the navigation planning, it is very uneconomical to increase the dredging depth and width.

4.2 *Impacts of dredging on the siltation*

We discussed the impacts of dredging on the siltation of the channel from the perspective of suspended sediment fluxes. On the longitudinal axis of the channel, the net sediment fluxes per unit width at Points 11–30 towards the downstream direction of the channel, with magnitudes increasing gradually (Fig. 7b). In a month, the sediment flux value for Case 3 (deepening) along the axis of the channel reaches 4.1 kg/s, and the values for Case 1, Case 2, and Case 4 are 2.9 kg/s, 2.8 kg/s, and 2.7 kg/s, respectively. The sediment fluxes decrease rapidly from Point 31 to Point 38, and the siltation thickness increases. The sediment fluxes at Points 7–10 in the channel point towards the upstream of the channel. So the suspended sediment in this section of the channel is transported landward; the deposition thickness at the channel head is larger. Regarding the upstream and downstream sections outside the channel, the scour depth increases and scour pits are formed. The suspended sediment fluxes decrease at Points 7–10 and increase at Points 11–38 after dredging; within the latter range, the increase is greater for Points 21–38. Therefore, compared to Case 0 (non-dredging), the variation in bed level at the landward section (Points 7–21) is larger than that in the seaward section (Points 22–38).

To analyze the sediment fluxes from the northern and southern shoals of the estuary into the channel, the monthly averaged sediment fluxes per unit depth from the southern and northern longitudinal sections of the channel were calculated (Fig. 8). Before dredging, the sediment moves into the channel through the northern section of the channel, and the maximum sediment

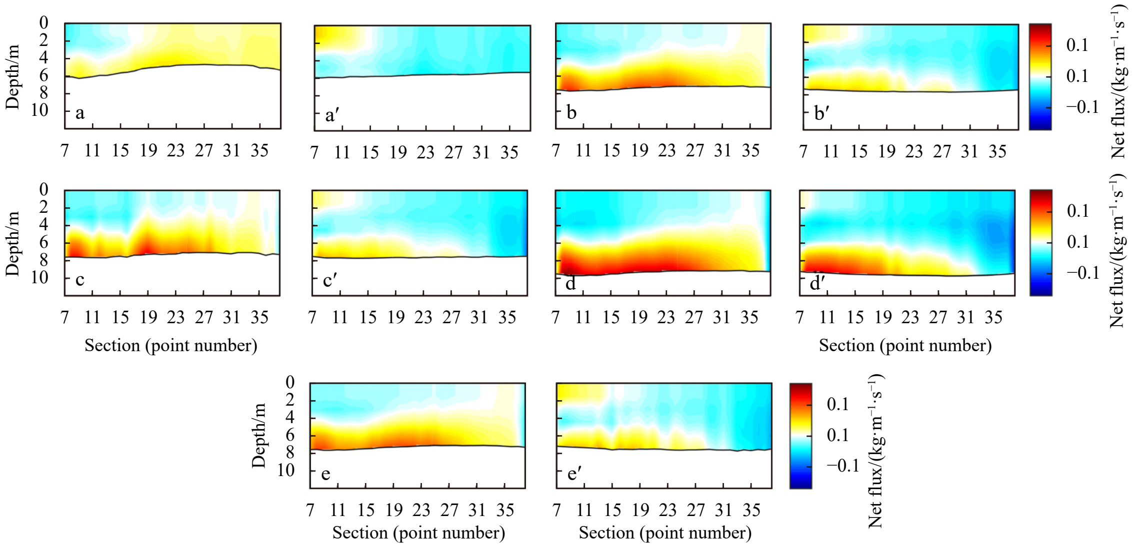

Fig. 8. Monthly averaged net sediment fluxes per unit depth to the channel at the north and south sections of the channel (positive values denote the fluxes pointing to the inside of the channel, while negative is opposite): north section for Case 0–Case 4 (a–e), and south section for Case 0–Case 4 (a′–e′).

fluxes reaches 0.050 kg/(m·s), while moves out of the channel through the southern section with maximum sediment fluxes –0.048 kg/(m·s). After dredging, due to the deflection of the bottom flow to the inner side of the channel, the bottom sediment fluxes into the channel at the northern and southern sections increase significantly. The suspended sediment fluxes exhibit a general trend wherein at the bottom level, they point towards the inner side of the channel, and at the surface level, they point towards the outer side. The suspended sediment fluxes from the northern section to the inner side of the channel are larger than those from the southern section. In the northern section, the maximum sediment fluxes per unit depth at the bottom for Case 1–Case 4 are 0.113 kg/(m·s), 0.135 kg/(m·s), 0.171 kg/(m·s), and 0.108 kg/(m·s), respectively. In the southern section, the values are 0.060 kg/(m·s), 0.064 kg/(m·s), 0.137 kg/(m·s), and 0.067 kg/(m·s), respectively; the flux value is the largest for Case 3 (deepening).

4.2.1 *Lateral sediment fluxes*

The change of channel geometry can change the sediment flux mechanism (Figueroa et al., 2020). The mechanism of monthly averaged net sediment fluxes in the east, west, north, and south sections of the dredged channel was determined (Table 4). The results reveals that the vertical net circulation transport is the primary contributor to channel dredging siltation, followed by the advection transport and the tidal pumping transport is relatively small.

After dredging, the vertical net circulation transport ($T_6 + T_7$) in the north and south sections increase significantly. Compared to Case 0 (non-dredging), the sediment fluxes for Case 1–Case 4 entering the channel at the north section increase by 682.1 kg/s, 634.2 kg/s, 1 024.6 kg/s, and 651.4 kg/s, respectively, and those at the south section increase by 610.4 kg/s, 609.2 kg/s, 942.8 kg/s, and 517.3 kg/s, respectively. Concerning the advection transport ($T_1 + T_2$), in the north section, the sediment fluxes entering the channel decrease by 165.2 kg/s, 178.0 kg/s, 185.4 kg/s, and 142.2 kg/s, respectively, for Case 1–Case 4. In the south section, the flux values for Case 1, Case 2, and Case 4 decrease by 47.1 kg/s, 96.7 kg/s, and 202.2 kg/s, respectively, and that for Case 3 increase by 70.4 kg/s.

The change in advection transport due to the change in the residual current is depicted in Fig. 9. After dredging, the residual currents near the bottom of the north section, towards the inner side of the channel, increase from 0.05 m/s for Case 0 to 0.07 m/s for dredging schemes. At the landward end of the south section, for Case 1 (Points 7–20), Case 2 (Points 7–21), Case 3 (Points 7–31), and Case 4 (Points 7–22), the inward-channel residual currents decrease/increase at the surface/bottom layer. The overall residual current points to the outer side of the channel. In addition, after dredging, SSC at the bottom level of the north and south sections decreases. The maximum reductions for Case 1–Case 4 in the north section are 0.09 kg/m^3, 0.08 kg/m^3, 0.16 kg/m^3, and 0.12 kg/m^3, respectively, and the maximum reductions for Case 1–Case 4 in the south section are 0.09 kg/m^3, 0.11 kg/m^3, 0.17 kg/m^3, and 0.15 kg/m^3, respectively. The reduced SSC and

Table 4. Contributions of different sediment transport parameters to the magnitude of absolute sediment transport of the four sections for Case 0–Case 4 (unit: kg/s)

		$T_1 + T_2$	$T_3 + T_4 + T_5$	$T_6 + T_7$
Case 0	N	913.0	67.1	87.5
	S	−1 012.0	−315.9	47.0
	W	90.0	−225.0	−2.4
	E	−25.5	−67.3	4.5
Case 1	N	747.8	−141.1	769.6
	S	−964.9	−499.9	657.4
	W	145.0	−217.0	−20.5
	E	−49.4	−130.1	−5.5
Case 2	N	738.0	−152.1	724.7
	S	−922.3	−574.2	659.2
	W	122.5	−182.5	−20.3
	E	−45.6	−124.2	−5.8
Case 3	N	730.6	−240.0	1 115.1
	S	−1 079.4	−520.7	992.8
	W	165.5	−190.5	−60.8
	E	−95.3	−193.6	−7.3
Case 4	N	770.8	−172.4	738.9
	S	−809.7	−250.9	564.3
	W	216.0	−252.0	−32.1
	E	−88.8	−200.4	−8.6

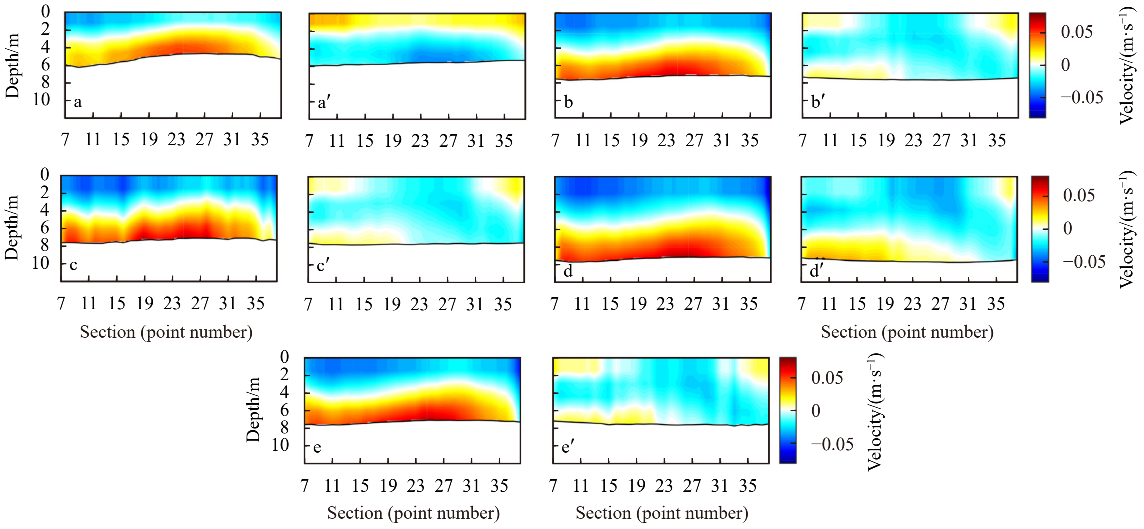

Fig. 9. Monthly averaged residual current component profile (positive values denote the fluxes pointing to the inside of the channel, while negative is opposite): north section for Case 0–Case 4 (a–e), and south section for Case 0–Case 4 (a'–e').

residual currents decrease the net sediment flux from the north section into the channel.

Although the vertical net circulation transport of the Jiaojiang River Estuary is smaller than other transport terms, it contributes substantially to channel siltation. After dredging, the bottom currents deflect to the inner side of the channel, and the surface currents deflect to the outer side of the channel. Therefore, the difference of horizontal current of each layer in water column increases. Since the surface SSC is less than the average vertical concentration while the bottom SSC is greater, the positive and negative values of $\overline{U}_{\rm v}$ and $\overline{C}_{\rm v}$ are consistent after dredging at bottom at the north section, which causes suspended sediment transport to the inside of the channel due to the vertical net circulation term. While in the south section, the values of $\overline{U}_{\rm v}$ and $\overline{C}_{\rm v}$ at the bottom level are positive or negative alternatively, the term $\overline{U}_{\rm v}\cdot\overline{C}_{\rm v}$ is still positive on the whole. Hence, the vertical net circulation term leads transport of suspended sediment into the channel.

To explain the mechanism of lateral circulation, Eq. (12) was used to calculate the contribution of each mechanism on the lateral circulation during flood and ebb in the spring tides. Point 9 (Fig. 1f) of the north section of the channel where the siltation thickness is large, was chosen to illustrate the result (Table 5; Fig. 10).

Before dredging, during the spring flood tide, the vertical frictional dissipation has the greatest impact on the lateral circulation, accounting for more than 50%. After dredging, the friction term has a decreased magnitude because of the increase of water depth. The non-linear advective term becomes the dominant force in driving the lateral circulation after dredging, which accounts for more than 50%. The Coriolis force, centrifugal force, and lateral baroclinic pressure gradient have small influence on the lateral circulation after dredging. During the spring and ebb tide, the trend is similar to that in the flood tide. The lateral circulation together with the higher bottom SSC controls the sediment fluxes at Point 9.

4.2.2 *Along channel sediment fluxes*

The sediment fluxes along channel are mainly controlled by the tidal pumping effect ($T_3 + T_4 + T_5$), which changes greatly after dredging (Fig. 11). Between Points 21–31, due to the sharp increase of ebb tidal current velocity, the tidal pumping transport increases significantly. Case 1 (dredging controlled) and Case 3 (deepening) increase by 1.12 kg/(m·s) and 1.65 kg/(m·s), respectively, compared with Case 0 (non-dredging). After Point 31, owing to the rapid decrease in the ebb tidal current, the sediment transport decreases rapidly, with Case 3 (deepening) demonstrating the most obvious change. This redistributes the sediment entering the channel.

In order to explore the mechanism of tidal pumping effect, we used Eq. (13) to calculate the tidal skewness. After the dredging, the $\rm M_2$ amplitude increases in the entire estuary compared to the non-dredging scheme. The phases are advanced. The amplitude of the shallow water tides is inversely proportional to the water depth. $\rm M_4$ amplitude decreases. The phases of $\rm M_4$ are advanced (Fig. 12). The changes in the $\rm M_2$ and $\rm M_4$ tidal amplitudes and phases cause the variations of the tidal asymmetry calculated by Eq. (13). The decrease of γ indicates that the dominant advantage of flood tide is weakened after channel dredging. This leads to an increase in downstream transport along the channel.

5 Conclusions

This study addresses the impacts of channel dredging on sediment dynamics in the Jiaojiang River Estuary, through using sediment data analysis and a well-calibrated FVCOM. Analysis of 51 bed sediment samples obtained near the estuarine channel reveals that the sediment is composed primarily of silty clay and clayey silt, with relatively fine grain sizes. Numerical modelling indicates that after dredging, the near-bottom flow around the channel deflects into the channel. The SSC of the shoals outside

Table 5. Contribution (%) of each forcing to the lateral circulation at the bottom level during the spring tides at Point 9

		Advection	Coriolis	Curvature	Sediment-induced baroclinic	Friction
Flood	Case 0	26.62	8.89	6.14	3.82	54.54
	Case 1	51.19	2.14	3.17	5.38	38.12
	Case 3	61.28	0.85	1.98	5.22	30.67
Ebb	Case 0	43.38	3.33	2.40	2.66	48.23
	Case 1	54.80	1.19	0.65	3.82	39.54
	Case 3	59.06	1.31	3.48	6.28	29.87

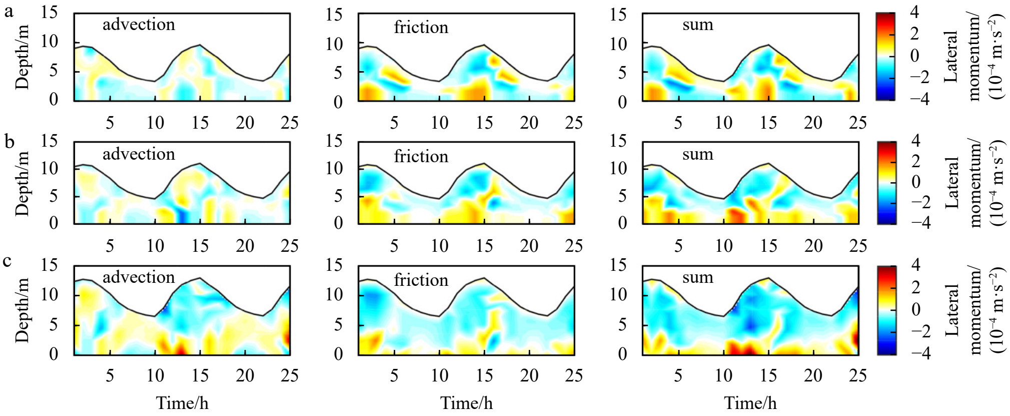

Fig. 10. Lateral momentum of times series at Point 9 during the spring tides (positive values denote the momentum pointing to the inside of the channel. while negative is opposite): Case 0 (a), Case 1 (b), and Case 3 (c).

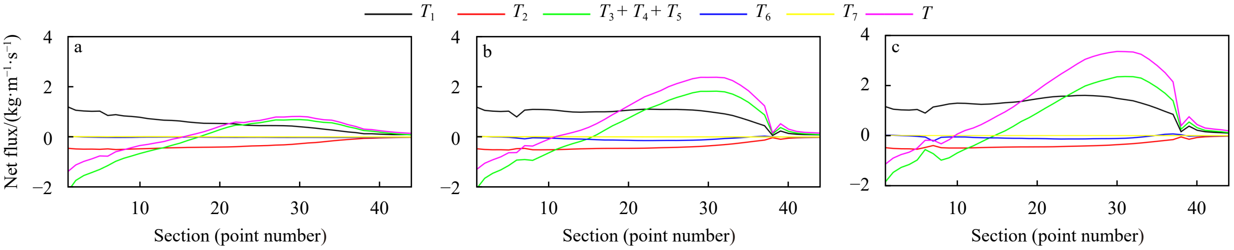

Fig. 11. Monthly averaged decomposition of suspended sediment flux per unit width along the channel (positive values indicate transport towards the downstream, while negative is oppsite): Case 0 (a), Case 1 (b), and Case 3 (c). The meaning of T_1, T_2, $T_3 + T_4 + T_5$, T_6 , T_7 are shown in Equation (12). T=T_1 + T_2 + T_3 + T_4 + T_5 +T_6 + T_7.

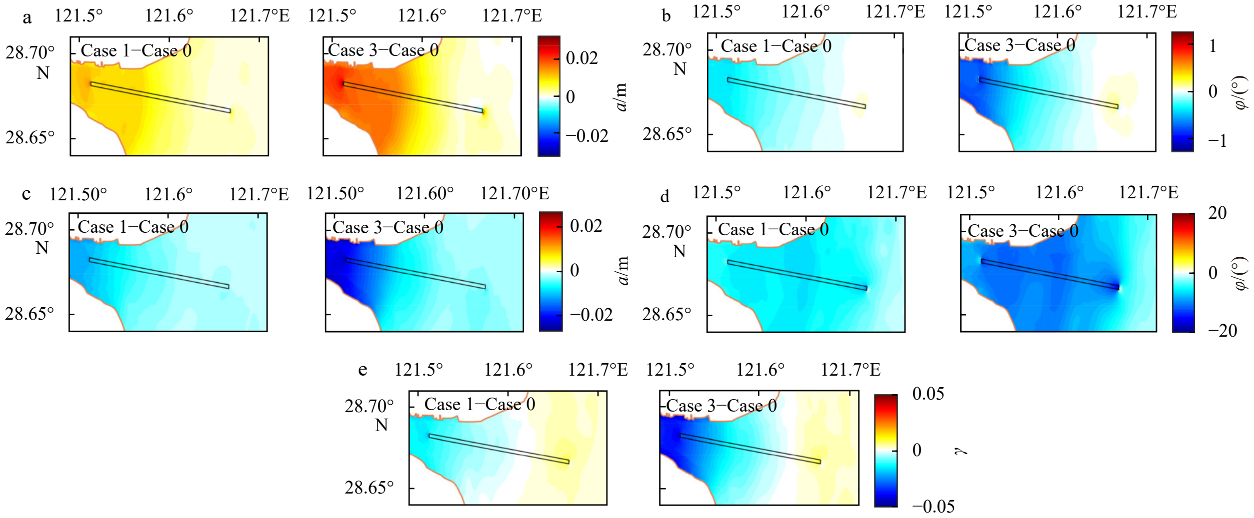

Fig. 12. M_2 tidal amplitude variation (a); M_2 tidal phase variation (b); M_4 tidal amplitude variation (c); M_4 tidal phase variation (d); tidal asymmetry variation (e).

the channel decreases because of the reduction in bottom stress. Scouring occurs on the beach-channel interface and the upstream and downstream sections of the channel. Siltation occurs in all the dredging schemes.

Siltation thickness increases with the increasing sediment fluxes under different dredging widths, depths and positions, with the maximum siltation thickness (0.15 m) in the deepening (by 11.4 m) case and minimum siltation thickness (0.07 m) in the moving parallel case. As for siltation and dredging ratio, the deepening (by 11.4 m) case exhibits the largest value (4.21%) and case of moving parallel presents the smallest value (2.83%). Lateral sediment fluxes of estuarine channels reveal that the increase of vertical net circulation transport is the major contributor to siltation after dredging. Non-linear advection, which accounts for more than 50% of lateral circulation, increases when the channel depth increases. The lateral circulation together with high bottom SSC controls the lateral sediment fluxes. Along channel sediment fluxes indicate that tidal pumping effect redistributes the sediment in the channel. Flood dominance is weakened after channel dredging, leading to an increase of downstream transport along the channel.

Hence, channel dredging needs careful plans as topographic changes of the estuary, which would essentially impact hydrodynamics and sediment dynamics.

References

Aubrey D G, Speer P E. 1985. A study of non-linear tidal propagation in shallow inlet/estuarine systems Part I: Observations. Estuarine, Coastal and Shelf Science, 21(2): 185–205, doi: 10.1016/0272-7714(85)90096-4

Chen Changsheng, Liu Hedong, Beardsley R C. 2003. An unstructured grid, finite-volume, three dimensional, primitive equation ocean model: application to coastal ocean and estuaries. Journal of Atmospheric & Oceanic Technology, 20(1): 159–186, doi: 10.1175/1520-0426(2003)020<0159:AUGFVT>2.0.CO;2

Dong Lixian, Wolanski E, Li Yan. 1997. Field and modeling studies of fine sediment dynamics in the extremely turbid Jiaojiang River Estuary, China. Journal of Coastal Research, 13(4): 995–1003

Dong Jia, Zhang Ningchuan. 2011. Sediment parameter selecting method and its application in sediment concentration research. Journal of Waterway and Harbor (in Chinese), 32(5): 321–328, doi: 10.3969/j.issn.1005-8443.2011.05.004

Dou Guoren. 1999. Incipient motion of coarse and fine sediment. Journal of Sediment Research (in Chinese), (6): 1–9, doi: 10.16239/j.cnki.0468-155x.1999.06.001

Dyer K R. 1997. Partially mixed and well-mixed estuaries. In: Dyer K R, ed. Estuaries: A Physical Introduction. 2nd ed. Chichester: John Wiley and Sons, 136–164

Egbert G D, Erofeeva S Y, Ray R D. 2010. Assimilation of altimetry data for nonlinear shallow-water tides: quarter-diurnal tides of the Northwest European shelf. Continental Shelf Research, 30(6): 668–679, doi: 10.1016/j.csr.2009.10.011

Figueroa S M, Lee G H, Shin H J. 2020. Effects of an estuarine dam on sediment flux mechanisms in a shallow, macrotidal estuary. Estuarine, Coastal and Shelf Science, 238: 106718, doi: 10.1016/j.ecss.2020.106718

Folk R L, Andrews P B, Lewis D W. 1970. Detrital sedimentary rock classification and nomenclature for use in New Zealand. New Zealand Journal of Geology and Geophysics, 13(4): 937–968, doi: 10.1080/00288306.1970.10418211

Ghosh L K, Prasad N, Joshi V B, et al. 2001. A study on siltation in access channel to a port. Coastal Engineering, 43(1): 59–74, doi: 10.1016/S0378-3839(01)00006-0

Gu Fengfeng. 2018. Analysis method on influential factors to navigation channel siltation in estuary high suspended sediment concentration zone. Yangtze River (in Chinese), 49(20): 8–12, doi: 10.16232/j.cnki.1001-4179.2018.20.002

Guo Leicheng, van der Wegen M, Roelvink J A, et al. 2014. The role of river flow and tidal asymmetry on 1-D estuarine morphodynamics. Journal of Geophysical Research: Earth Surface, 119(11): 2315–2334, doi: 10.1002/2014JF003110

Huang Zhiyang. 2007. Research on the deposition of Lianyungang's deep-water navigation channel on muddy coast (in Chinese) [dissertation]. Nanjing: Hoihai University

Jin Liu. 2019. Influences of fine sediment transport and transversal sediment transport between shoal and channel on channel siltation. Port & Waterway Engineering (in Chinese), (8): 111–116, doi: 10.16233/j.cnki.issn1002-4972.20190805.018

Kalkwijk J P T, Booij R. 1986. Adaptation of secondary flow in nearly-horizontal flow. Journal of Hydraulic Research, 24(1): 19–37, doi: 10.1080/00221688609499330

Li Mengguo, Mai Miao, Li Wendan, et al. 2015. Study on harbor-constructing conditions in Jiaojiang River Estuary and Taizhou Bay. Journal of Waterway and Harbor (in Chinese), 36(5): 369–377

Li Yan, Pan Shaoming, Shi Xiaodong, et al. 1992. Recent sedimentary rates for the zone of the turbidity maximum in the Jiaojiang River Estuary. Journal of Nanjing University: Natural Sciences Edition (in Chinese), 28(4): 623–632

Liu Haoran, Xu Kehui, Wilson C. 2020. Sediment infilling and geomorphological change of a mud-capped Raccoon Island dredge pit near Ship Shoal of Louisiana shelf. Estuarine, Coastal and Shelf Science, 245: 106979, doi: 10.1016/j.ecss.2020.106979

Martelo A F, Trombetta T B, Lopes B V, et al. 2019. Impacts of dredging on the hydromorphodynamics of the Patos Lagoon estuary, southern Brazil. Ocean Engineering, 188: 106325, doi: 10.1016/j.oceaneng.2019.106325

Mateo-Pérez V, Corral-Bobadilla M, Ortega-Fernández F, et al. 2020. Port bathymetry mapping using support vector machine technique and sentinel-2 satellite imagery. Remote Sensing, 12(13): 2069, doi: 10.3390/rs12132069

Nguyen V T, Zheng Jinhai, Zhang Jisheng. 2013. Mechanism of back siltation in navigation channel in Dinh An Estuary, Vietnam. Water Science and Engineering, 6(2): 178–188, doi: 10.3882/j.issn.1674-2370.2013.02.006

Obelcz J, Xu Kehui, Bentley S J, et al. 2018. Mud-capped dredge pits: An experiment of opportunity for characterizing cohesive sediment transport and slope stability in the northern Gulf of Mexico. Estuarine, Coastal and Shelf Science, 208: 161–169, doi: 10.1016/j.ecss.2018.04.039

Shen Qi, Huang Wenrui, Wan Yuanyang, et al. 2020. Observation of the sediment trapping during flood season in the deep-water navigational channel of the Changjiang Estuary, China. Estuarine, Coastal and Shelf Science, 237: 106632, doi: 10.1016/j.ecss.2020.106632

Song Dehai, Wang Xiaohua, Kiss A E, et al. 2011. The contribution to tidal asymmetry by different combinations of tidal constituents. Journal of Geophysical Research: Oceans, 116(C12): C12007, doi: 10.1029/2011JC007270

van Prooijen B C, Winterwerp J C. 2010. A stochastic formulation for erosion of cohesive sediments. Journal of Geophysical Research: Oceans, 115(C1): C01005, doi: 10.1029/2008JC005189

Wang Xiaohua. 2002. Tide-induced sediment resuspension and the bottom boundary layer in an idealized estuary with a muddy bed. Journal of Physical Oceanography, 32(11): 3113–3131, doi: 10.1175/1520-0485(2002)032<3113:TISRAT>2.0.CO;2

Wang Gaoyang. 2007. A 2D numerical simulation of suspended sediment in the Taizhou Bay (in Chinese) [dissertation]. Hangzhou: Zhejiang University

Wang Xiaohua, Byun D S, Wang Xingli, et al. 2005. Modelling tidal currents in a sediment stratified idealized estuary. Continental Shelf Research, 25(5–6): 655–665, doi: 10.1016/j.csr.2004.10.013

Wang Yaping, Gao Shu, Jia Jianjun. 2000. Flow structure in the marine boundary layer and bedload transport: A review. Marine Geology and Quaternary Geology (in Chinese), 20(3): 101–106, doi: 10.16562/j.cnki.0256-1492.2000.03.016

Winterwerp J C. 2001. Stratification effects by cohesive and noncohesive sediment. Journal of Geophysical Research: Oceans, 106(C10): 22559–22574, doi: 10.1029/2000JC000435

Wu Teng, Li Xiuxia. 2010. Vertical 2-d mathematical model of sediment silting in dredged channel. Journal of Hydrodynamics, 22(1): 605–609, doi: 10.1016/S1001-6058(10)60005-4

Wu Hui, Shen Jian, Zhu Jianrong, et al. 2014. Characteristics of the Changjiang plume and its extension along the Jiangsu Coast. Continental Shelf Research, 76: 108–123, doi: 10.1016/j.csr.2014.01.007

Xu Xuesong, Zhang Xinzhou, Li Qiong, et al. 2018. Simulation on flow-sediment characteristic and turbidity maximum zone in Jiao (Ling) River. Port & Waterway Engineering (in Chinese), (12): 134–142, doi: 10.16233/j.cnki.issn1002-4972.20181130.004

Ye Taoyan, Li Li, Wang Yongxue, et al. 2019. Impacts of tidal flat reduction on suspended sediment dynamics in Hangzhou Bay. Journal of Tianjin University (Science and Technology) (in Chinese), 52(4): 392–403, doi: 10.11784/tdxbz201804092

Zhang Hongwei. 2006. A two dimentional modeling suspended solids in the estuary of Jiaojiang River (in Chinese) [dissertation]. Hangzhou: Zhejiang University

Zhao Xiaodong, Li Xiaoxiao, Luo Xiaofeng, et al. 2014. Study on the sediment deposition in Yuanyuansha reach of 12.5 m deepwater channel in Yangtze Estuary. Journal of Sediment Research (in Chinese), (6): 63–67, doi: 10.16239/j.cnki.0468-155x.2014.06.011

Zhu Yongkang. 1986. Some characteristics of the Jiao Jiang mountain river estuary under strong tides in Zhejiang province. Geographical Research (in Chinese), 5(1): 21–31

Zhu Jun, Weisberg R H, Zheng Lianyuan, et al. 2015. Influences of channel deepening and widening on the tidal and nontidal circulations of Tampa bay. Estuaries and Coasts, 38(1): 132–150, doi: 10.1007/s12237-014-9815-4

Zhu Qin, Yang Shilun, Ma Yanxia. 2014. Intra-tidal sedimentary processes associated with combined wave-current action on an exposed, erosional mudflat, southeastern Yangtze River Delta, China. Marine Geology, 347: 95–106, doi: 10.1016/j.margeo.2013.11.005

Žilinskas G, Janušaitė R, Jarmalavičius D, et al. 2020. The impact of Klaipėda Port entrance channel dredging on the dynamics of coastal zone, Lithuania. Oceanologia, 62(4): 489–500, doi: 10.1016/j.oceano.2020.08.002